

Modulating Hierarchical Self-Assembly In Thermoresponsive Intrinsically Disordered Proteins Through High-Temperature Incubation Time

*Vaishali Sethi^{1,2,3}, Dana Cohen-Gerassi^{2,3,4}, Sagi Meir^{1,2,3}, Max Ney⁵, Yulia Shmidov⁵, Gil
Koren^{1,2,3}, Lihi Adler-Abramovich^{2,3,4}, Ashutosh Chilkoti⁵, and Roy Beck^{*1,2,3}*

¹ Raymond and Beverly School of Physics and Astronomy, Tel Aviv University, Tel Aviv
6997801, Israel.

² The Center for Physics and Chemistry of Living Systems, Tel Aviv University, Tel Aviv
6997801, Israel.

³ The Center for Nanoscience and Nanotechnology, Tel Aviv University, Tel Aviv 6997801,
Israel.

⁴ Department of Oral Biology, The Goldschleger School of Dental Medicine, Sackler Faculty of
Medicine, Tel Aviv University, Tel Aviv 6997801, Israel.

⁵ Department of Biomedical Engineering, Duke University, Durham, NC 27708, USA

Abstract

The cornerstone of structural biology is the unique relationship between protein sequence and the 3D structure at equilibrium. Although intrinsically disordered proteins (IDPs) do not fold into a specific 3D structure, breaking this paradigm, some IDPs exhibit large-scale organization, such as liquid-liquid phase separation. In such cases, the structural plasticity has the potential to form numerous self-assembled structures out of thermal equilibrium. Here, we report that high-temperature incubation time is a defining parameter for micro and nanoscale self-assembly of resilin-like IDPs. Interestingly, high-resolution scanning electron microscopy micrographs reveal that an extended incubation time leads to the formation of micron-size rods and ellipsoids that depend on the amino acid sequence. More surprisingly, a prolonged incubation time also induces amino acid composition-dependent formation of short-range nanoscale order, such as periodic lamellar nanostructures. We can correlate the lamellar structures to β -sheet formation and demonstrate similarities between the observed nanoscopic structural arrangement and spider silk. We, therefore, suggest that regulating the period of high-temperature incubation, in the one-phase regime, can serve as a unique method of controlling the hierarchical self-assembly mechanism of structurally disordered proteins.

Introduction

The organization of macromolecules into compartments allows cells tight regulation of physiological functions. In addition to classical membrane-bound organelles, eukaryotic cells also form dynamic, liquid-like membrane-less organelles (MLOs) to orchestrate biochemical reactions and cellular stress effectively.¹⁻³

Intrinsically disordered proteins (IDPs) have significant stretches in their primary amino acid sequence-termed intrinsically disordered regions (IDRs) that lack a singular, stable 3D structure.⁴⁻⁷ Such IDPs have attracted significant attention as hubs of protein-interaction networks that regulate transcription, translation, cell cycle⁸⁻¹⁰, and modulate intracellular signaling.¹¹⁻¹³ In addition, liquid-liquid phase separation (LLPS) of IDPs has been shown to play an important role in the formation of MLOs,¹⁴⁻¹⁶ and dysregulation of LLPS due to irreversible aggregation of IDPs can lead to a variety of pathological diseases.¹⁷⁻¹⁹

The LLPS of IDPs has also enabled diverse applications ranging from protein purification²⁰, drug delivery²¹⁻²³, self-assembly of artificial MLOs into nano-meso structures²⁴⁻²⁶, to injectable biomaterials and hydrogels.²⁷⁻²⁹ Importantly, beyond the sequence, other external stimuli, such as pH, protein concentration, and temperature, have also been shown to affect LLPS.³⁰

Like synthetic polymers, IDPs can also exhibit thermoresponsive phase behavior, controlled by the spatial orientation of amino acid side chains and peptide-water interactions.³¹⁻³³ IDPs with an upper critical solution temperature (UCST) undergo LLPS below their transition temperature (T_t), also called the cloud point temperature. At high temperatures ($T > T_t$), the system is a homogenous solution, while at lower temperatures, it exists as a two-phase system consisting of an IDP-rich coacervate phase (immiscible in water) and a dilute phase of IDPs dissolved in the solvent. The UCST phase -separation is reversible, and above the T_t , the coacervates become soluble again.^{20,34} In contrast, other IDP sequences with a lower critical solution temperature (LCST) exhibit phase separation above their cloud point temperature.³⁴ Examples of UCST and LCST IDP-based thermoresponsive polymers are resilin-like polypeptides (RLPs)³³ and elastin-like polypeptides (ELPs)³⁴, derived from the disordered sequences of the natural proteins resilin³⁵ and tropoelastin³⁶, respectively.

Designing new strategies to drive the self-assembly of resilin-like IDPs is important in light of their possible applications in tissue engineering, bioelectronics, bioimaging and biosensors.³⁷ Here, we investigate the thermoresponsive behavior and self-assembly of RLPs, a class of synthetic intrinsically disordered proteins (SynIDPs) derived from resilin.³⁵ We focus on their self-assembly into nano- and micro-scale structures modulated by changes in incubation time at temperatures above the LLPS transition temperature. In addition, we show that it is possible to fine-tune the resulting self-assembled structures by alterations in the sequence and the number of repeats of the RLPs.

Results

This study investigated the hierarchical self-assembly of SynIDPs derived from a 8 amino acid repeats (GRGDSPYS) inspired by the *Drosophila Melanogaster* Rec-1 resilin protein, which exhibits UCST phase behavior.²⁰ Here, we focused on three RLPs, the octapeptide parent sequence is known as Wild type (WT), while the notation for the RLPs are [WT]_{XX}, where XX represents the number of octapeptide repeats in the SynIDPs, for example, [WT]₄₀ and [WT]₈₀. Further, the terminology of mutant versions of the RLPs is according to the position and type of amino acids that is substituted for the amino acid into the WT octapeptide repeat. For example, the mutant [V₇]₄₀ has V substituted for the Y at the 7th position in the octapeptide WT repeat. Specifically, we examined the effect of incubation time at 80° C (t_{80}), varying the number of octapeptide repeats and changing the sequence of the SynIDPs. All studied RLPs sequences are presented in Table 1.

Table 1. Characteristics of the A-IDP sequences

Protein name	Sequence	No. of amino acids	Molecular weight (Da)
[WT] ₂₀	SKGP-(GRGDSPYS) ₂₀ -GY	166	17,004
[WT] ₄₀	SKGP-(GRGDSPYS) ₄₀ -GY	326	33,400
[WT] ₆₀	SKGP-(GRGDSPYS) ₆₀ -GY	486	49,797
[WT] ₈₀	SKGP-(GRGDSPYS) ₈₀ -GY	646	66,193
[3Y ₇ V ₇] ₄₀	SKGP-[(GRGDSPYS) ₃ GRGDSPVS] ₁₀ -GY	326	32,760
[Y ₇ V ₇] ₄₀	SKGP-[GRGDSPYSGRGDSPVS] ₂₀ -GY	326	32,119
[V ₇] ₄₀	SKGP-(GRGDSPVS) ₄₀ -GY	326	30,839

Microscale self-assembly

Previous reports suggest that RLPs [WT]₄₀, and [WT]₈₀, show reversible LLPS below the cloud point, $T_c = 40^\circ\text{C}$, when measured in 150 mM phosphate buffer of pH 7.4.²⁰ Both [WT]₄₀ and [WT]₈₀ RLPs are insoluble when prepared in buffer at 25°C. However, these samples do show LLPS after incubation at 80°C for $t_{80} = 1$ h and cooling back to 25°C. In contrast, the mutant [V₇]₄₀ did not show such reversible UCST phase behavior and remained insoluble after 1 h of incubation at 80°C.

We investigated the effect of incubation time on the microscale self-assembly of [WT]₄₀, [WT]₈₀, and [V₇]₄₀ by incubating 100 μM solutions of the RLPs in 150 mM phosphate buffer at 80°C for 1, 24, and 48 h. After incubation, the solutions were cooled back to 25°C for 10 min. For convenience, we term a sample with XX repeats incubated at 80°C for t_{80} hours and measured at 25°C as [sample]_{XX- t_{80}} .

High-resolution scanning electron microscopic (HRSEM) was used to characterize the morphology of the microstructures after different incubation times (Figs. 1-3). Before hydration and self-assembly, the HRSEM images of [WT]₄₀ powder samples are amorphous (Fig. 1a). However, after hydration and 1 h incubation at high temperature, images show that [WT]₄₀ are predominantly composed of 400 nm wide and ~600 nm long micro-ellipsoids with a few ~ 500 nm diameter rods that are several μm in length (Fig. 1b). A more prolonged incubation ($t_{80} = 24$ h), increased the number of rods in this system (Fig. 1c).

Longer incubation ($t_{80} = 48$ h) produced an interconnected system of rods ~ 500 nm wide, but with length in microns (Fig. 1c). These rods appear to be formed due to the systematic arrangement of ellipsoidal particles through inter-connecting nanofibers (arrows in Fig. 1b & Supplementary Fig. S1a).

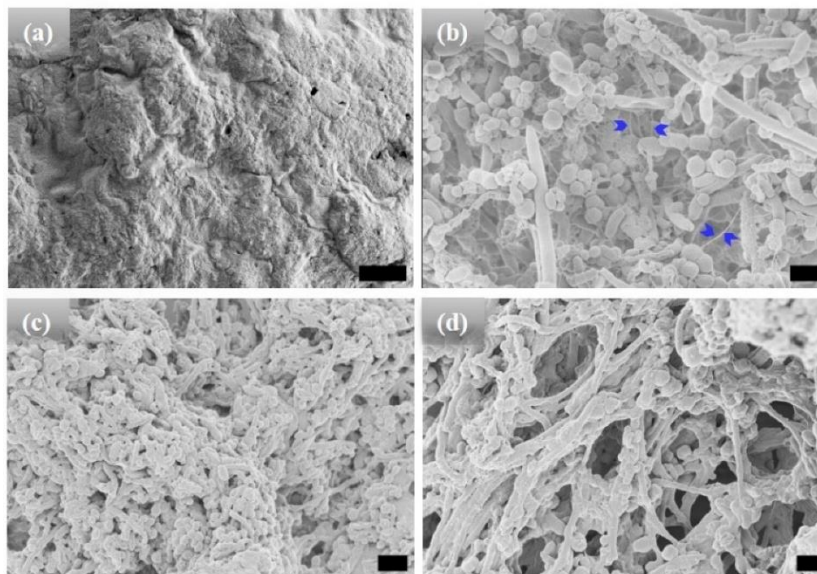


Figure 1. HRSEM micrographs of $[WT]_{40}$ RLP (a) amorphous powder samples. (b)-(d) $[WT]_{40}$ in phosphate buffer solutions after incubation at 80°C for 1, 24, and 48 h, respectively. Incubation for 1 h results in the formation of micro-ellipsoids of 500 nm width and ~ 1 μm in length and a few rods of ~ 500 nm in diameter and several μm in length (b). A longer incubation of 24 h leads to an increase in the micro-rod population (c). A 48 h incubation produced microstructures with interconnected rods (d). Arrows in (b) mark interconnecting nanofibers, which leads to self-assembly of micro-ellipsoids to form micro-rods. Scale bar: $1\mu\text{m}$.

The $[WT]_{80}$ powder samples also exhibit an amorphous structure (Fig. 2a). However, imaging revealed that a hydrated $[WT]_{80}$ solution undergoes LLPS after incubation at 80°C for 1 h, with the formation of condensates of several μm in length (Fig. 2b). Micro-rods and micro-ellipsoids were only seen after incubating the $[WT]_{80}$ peptide in buffer solution for 24 h at 80°C (Fig. 2c). Similar to $[WT]_{40}$ RLP incubated for 48 h, $[WT]_{80}$ -24 h sample also exhibits interconnecting nanofibers between the micro-ellipsoids which connect together to form micron size rods (Supplementary Fig. S1b). Thus, in both $[WT]_{40}$ and $[WT]_{80}$ systems, 48 h of incubation at 80°C induced the formation of long rods accompanied by a few micro-ellipsoids (Figs. 1d, 2d).

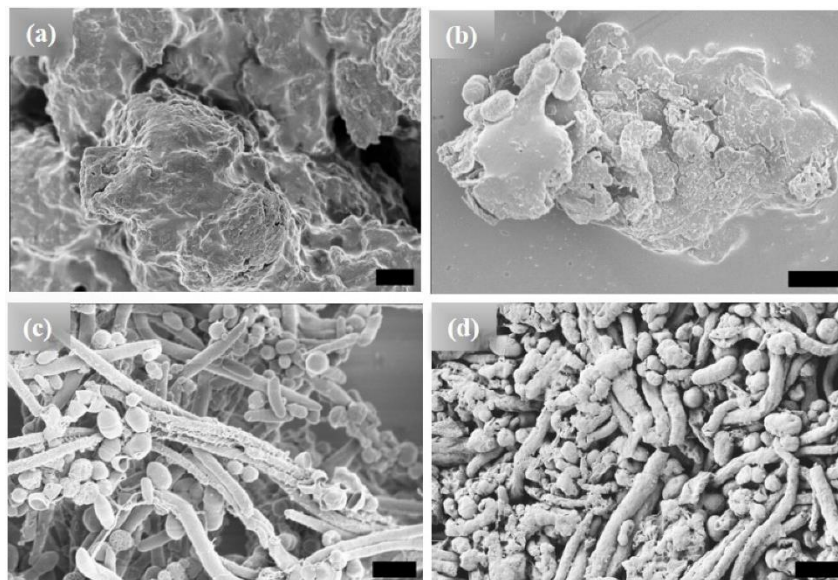


Figure 2. HRSEM images of $[WT]_{80}$ RLP (a) amorphous powder samples. Micrographs of RLP solutions in buffer after incubation at 80°C . (b) A 1h incubation results in the formation of several μm long condensates, (c) 24 h incubation produces a mixture of micro-rods and micro-ellipsoids, and (d) 48 h incubation results in several μm long micro-rods accompanied by some micro-ellipsoids. Scale bar: $1\mu\text{m}$.

Unlike the $[WT]$ RLPs, a powder sample of $[V_7]_{40}$ does not undergo LLPS and exhibits an amorphous structure (Fig. 3a). The sample remained amorphous after 1 and 24h incubation at 80°C (Fig. 3b & c respectively) and only after extended incubation at high temperature (i.e., $t_{80} = 48$ h), the sample become turbid and exhibit ellipsoidal particles that were $\sim 500\text{nm}$ in width and ~ 650 nm in length as observed by HRSEM with a few several μm long rods (Fig. 3d). Unlike $[WT]_{40}$, the primary morphology observed for $[V_7]_{40}$ after 48 h incubation is micro-ellipsoidal rather than elongated rods.

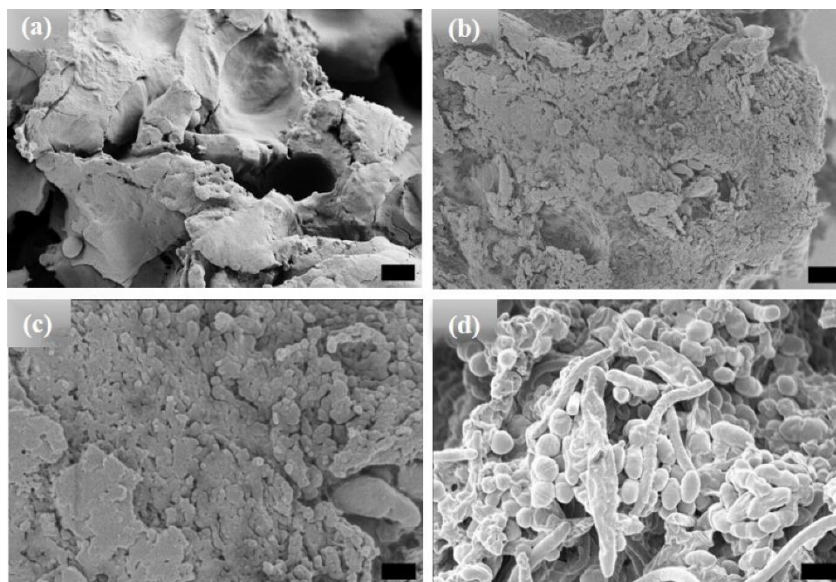


Figure 3. HRSEM images of $[V_7]_{40}$ RLP (a) powder samples, (b)-(d) $[V_7]_{40}$ RLP solutions after incubation at 80°C for 1, 24, and 48 h, respectively. The powder samples and solutions incubated for 1 and 24 h have an amorphous structure, but micro-ellipsoids accompanied by few nanorods are observed after 48 h incubation at 80°C . Scale bar: $1\mu\text{m}$.

Nanoscope Self-Assembly

Motivated by the microscale self-assembly of SynIDPs and the correlation with incubation time, we used small- and wide-angle X-ray scattering (SAXS, WAXS) techniques to investigate the nanoscopic structures.^{38,39} RLP samples and excess supernatant were sealed in polycarbonate capillaries and placed into a measurement heating stage. This allowed temperature dependent investigation of the samples with the desired high temperature incubation. For phase separated samples the X-ray scattering measurements is of the pellet positioned at the bottom of the capillary. The lack of correlation peaks in the scattering profiles of $[WT]_{40}$, $[WT]_{80}$, and $[V_7]_{40}$ solutions after 1 h incubation (Fig. 4a) indicate that the structure is amorphous with no long- or short-range repeated order. Notably, there was no order in lyophilized powders of these A-IDPs (Supplementary Fig. S2a).

To our surprise, incubation of $[WT]_{80}$ peptide solutions for $t_{80} = 24$ h resulted in the appearance of two sharp correlation peaks (i.e., q_a and q_b) in the scattering profile (Fig. 4b). Such scattering peaks indicate the presence of repeated nanoscopic structures. Increasing the incubation time to 48 h produced intense correlation peaks only in the $[V_7]_{40}$ -48 h system (Figs. 4c & 4d). Interestingly, the scattering profiles of $[3Y_7V_7]$ and $[Y_7V_7]$, where 25% and 50% of Y are replaced by V, respectively, do not exhibit correlation peaks after 48 h incubation (Supplementary Fig. S2b). Therefore, we can conclude that the both the sequence and incubation time ultimately dictate the nanoscopic long- or short-range self-assembly in

RLPs considered for our studies. Specifically, the scattering profile of the $[V_7]_{40-48}$ h system exhibits six correlation peaks ($q_1, q_2, q_4, q', q_{\beta_1}$, and q_{β_2} , Fig. 4d) where the positions of peaks q_1, q_2 and q_4 are in the ratio $q_1:2q_1:4q_1$ and $q_1 = 1.082 \text{ nm}^{-1}$. This profile indicates the presence of an ordered lamellar morphology corresponding to an interplanar distance of 5.8 nm. In addition, there was a strong singular correlation peak, $q' = 1.646 \text{ nm}^{-1}$, without any additional harmonics (Fig. 4d). The spacing of the correlation peaks at $q_{\beta_1} = 15.09 \text{ nm}^{-1}$ and $q_{\beta_2} = 15.4 \text{ nm}^{-1}$, corresponding to real space distances of 0.416 nm (d_{β_1}) and 0.406 nm (d_{β_2}), which is typical of protein secondary structure (Fig. 4d).

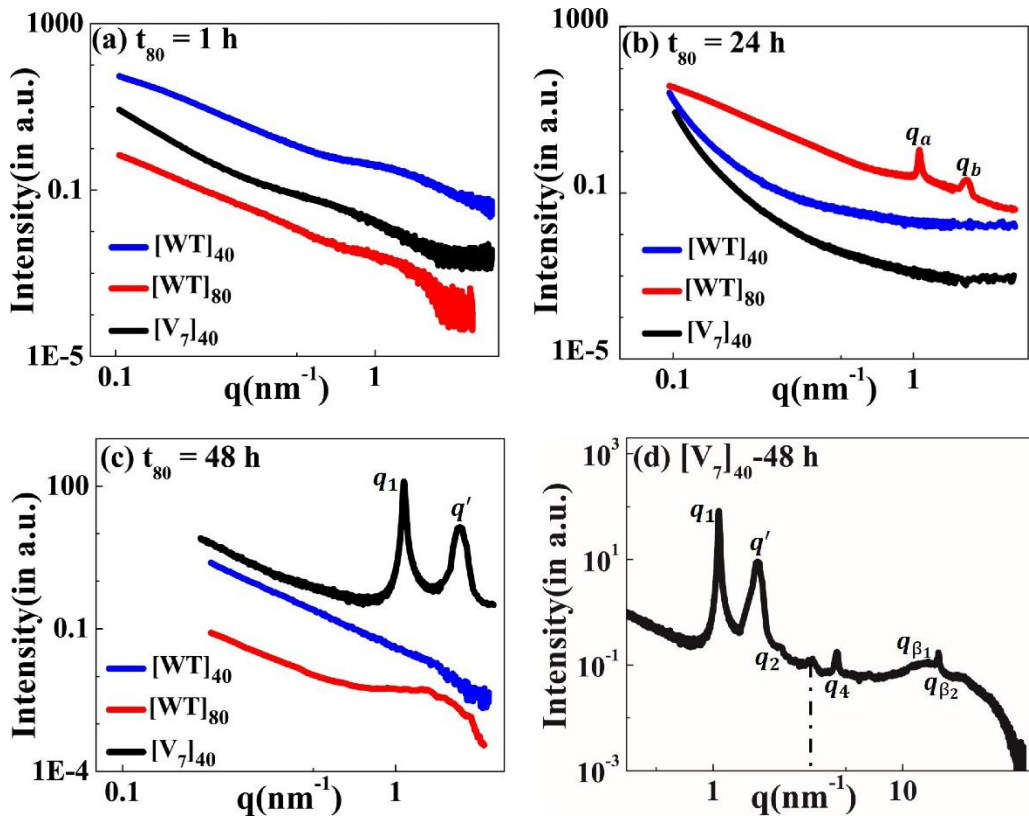


Figure 4. The scattering profiles of the $[WT]_{40}$, $[WT]_{80}$, and $[V_7]_{40}$ RLPs after incubation at 80°C (t_{80}) for the duration of (a) 1 h, (b) 24 h, and (c) 48 h. There were no correlation peaks after 1 h but $[WT]_{80-24}$ h and $[V_7]_{40-48}$ h RLPs exhibit two intense correlation peaks q_a, q_b and q_1, q' respectively, indicative of nanoscopic long- or short-range ordering (d) Extended scattering profile of the $[V_7]_{40-48}$ h RLP exhibiting lamellar peaks (q_1, q_2, q_4), and a singular correlation peak (q') with no additional reflections, and peaks corresponding to the secondary structure of proteins (q_{β_1} and q_{β_2}). The peak at $q \sim 3.4 \text{ nm}^{-1}$ (shown by a dotted line) corresponds to a residual diffraction peak of the kapton window originating from the experimental setup.⁴⁰

Previous measurements described the H-bonding distance between antiparallel strands of the β -sheets of some nylons to be 0.474 nm .^{41,42} In line with that, we presume that in our $[V_7]_{40-48}$ h system, the

correlation peak q_{β_2} arises due to repetitive arrangement of β -strands through backbone H-bonds with inter-strand spacing of d_{β_2} (0.406 nm). Further, the reported inter-sheet distances between stacked β -sheets ranges from a minimum of 0.34 nm for poly(Gly)⁴³ to a maximum of 0.79 nm for Nephila Senegalese silk fibroin, a silk that contains a high percentage of amino acid residues with bulky side chains.⁴⁴ Therefore, the $d_{\beta_1} = 0.416$ nm spacing we observed corresponds to an average inter-sheet distance between stacked β -sheets.

To validate the presence of secondary structure, we performed circular dichroism (CD) studies for $[V_7]_{40}$ systems after various incubation times at high temperatures. We acknowledge that for IDPs, the analysis of CD spectra is limited, since current models were derived based on folded proteins.^{45,46} Nonetheless, after one hour of incubation the $[V_7]_{40}$ -1h RLP exhibits a peak at 197nm and rather flat spectrum through rest of wavelength considered. This is because $[V_7]_{40}$ -1h sample is insoluble in phosphate buffer. Thus, it's not possible to predict secondary structures from the CD spectra of $[V_7]_{40}$ -1h sample with certainty (Fig. 5a).

Following 48 h incubation, the $[V_7]_{40}$ RLP did develop the characteristic valleys at ~ 203 and 225 nm and a peak at 190 nm corresponding to β -type structures (Fig. 5a) in correlation with the scattering profiles demonstrating antiparallel β -strands through backbone H-bonds (Fig. 4d). Similar CD spectra is previously reported for the β -sheets of Bombyx mori silk solution in hexafluoroisopropyl alcohol.⁴⁷

Acknowledging its limitation for IDPs, we used the BestSel algorithm to quantify the different types of secondary structures in the $[V_7]_{40}$ -48 h RLP.⁴⁶ The quantification confirmed that the $[V_7]_{40}$ RLP after 48hrs of incubation exhibit a mixture of secondary structures including α -helix, parallel and antiparallel β -sheets, turns, and disordered coils (Supplementary Fig. S3), while the predominant structures are antiparallel β -sheets (34%, Supplementary Fig. S3). The CD data agree with the WAXS data in finding β -sheets correlation peaks for the $[V_7]_{40}$ -48 h system (Fig. 4d).

Fourier transform infrared (FTIR) measurements for $[V_7]_{40}$ -1h and $[V_7]_{40}$ -48h further supported the secondary structure determination. Indeed for the 48 h incubation we find the amide I band at 1637cm^{-1} (corresponding to C=O stretch of peptide linkages) and amide II band at 1522cm^{-1} (mainly derived from in-plane NH bending) corresponds to β -sheets (Fig. 5b).⁴⁸ The higher wavenumber band at 1732cm^{-1} corresponds to antiparallel β -sheets in the system in support with our CD and X-ray data. No such bands are observed in FTIR spectra of $[V_7]_{40}$ -1hr sample (Fig. 5b), which confirms that incubation of 48hrs at 80°C lead to stabilization of antiparallel β -sheets in $[V_7]_{40}$ system.

In support of our experimental results, alphafold2⁴⁹ predicts completely disordered structure for [WT]₄₀ system (Supplementary Figs. S4a) which is in fact is the characteristic of IDP. On the contrary, alphafold2 for [V7]₄₀ shows more than 90% probability of presence of β -sheets (Supplementary Fig. S4b).

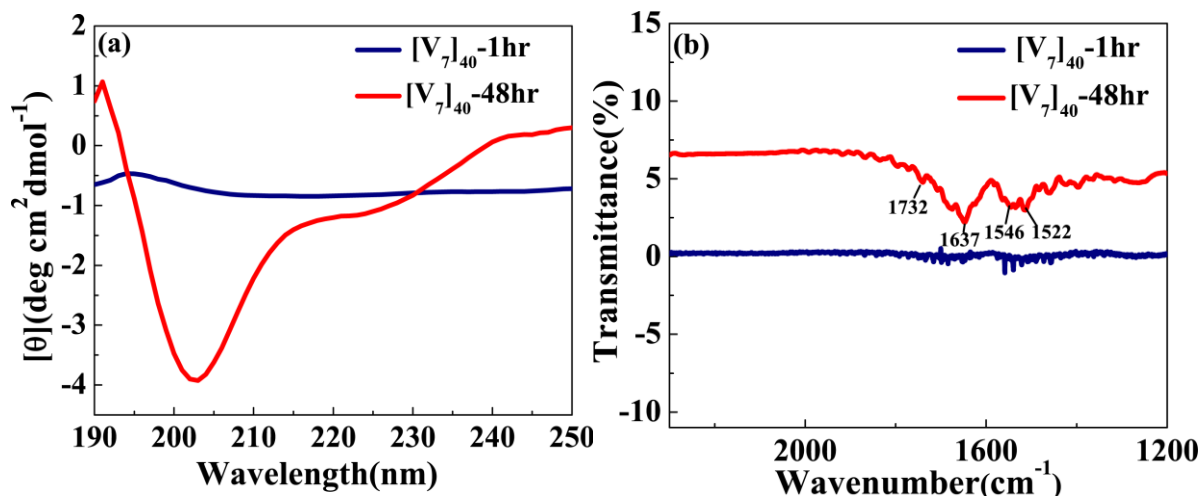


Figure 5. (a) CD spectra for [V₇]₄₀ RLP (a) After 1 and 48 hr incubation. The [V₇]₄₀-48hrs sample exhibits profile with valleys at the wavelengths of ~203 nm and ~225nm and a peak at 190nm characteristic to β -sheets. (b) FTIR spectra of [V₇]₄₀-1hr and [V₇]₄₀-48hr sample. The presence of infrared bands at 1522, 1637 and 1732 cm^{-1} in [V₇]₄₀-48hr sample confirms the presence of antiparallel β -sheets.

Next, we used X-ray scattering to investigate the temperature-dependence phase behavior of the lamellar structure in the [V₇]₄₀-48 h samples during the heating and cooling cycle. The experiment involves incubating at 80°C for t_{80} hours and then cooling back to 25°C. The temperature ramped up to 80°C with a ramp rate of 1°C min^{-1} during the heating cycle. After every 5°C increment, the system was held at the given temperature for 15 min for equilibration before collecting the scattering profiles (Supplementary Fig. S5). Scattering profiles were collected every 5°C during the cooling cycle from 80°C to 20°C (Supplementary Fig. S6).

The results indicate that while heating the [V₇]₄₀-48 h sample from 25°C-45°C, the lamellar correlation peaks systematically shift towards higher q -values. However, at temperatures above 45°C, the higher-order lamellar harmonics (q_{2H} , q_{4H}) and β -sheet peaks disappear ($q_{\beta_{1H}}$, $q_{\beta_{2H}}$) while the principal lamellar peak (q_{1H}), persists (Fig. 6a & Supplementary Fig. S5). Further heating the system to 50°C, causes q_{1H} to split into two peaks, where we designate the daughter peak as q_{1H}^* . Surprisingly, on further heating peak q_{1H} disappears at 55°C, while q_{1H}^* persists. From 60°C to 80°C (the maximum temperature reached in our experiment), q_{1H}^* completely disappears (Fig. 6a). Above 60°C, the last ordered structure signature is the correlation peak of q'_H that also remains in the one-phase regime (Fig. 6a & Supplementary Fig. S5). Further details of q'_H will be discussed in the subsequent section.

There were no signs of lamellar or β -sheet correlation peaks when the temperature of the $[V_7]_{40-48}$ h sample was decreased from 80 to 50°C during the cooling cycle (Fig. 6b & Supplementary Fig. S6). However, once the temperature reaches 45°C, we observe a single reflection, denoted as q_{1C}^* , in the SAXS region (Fig. 6b & Supplementary Fig. S6).

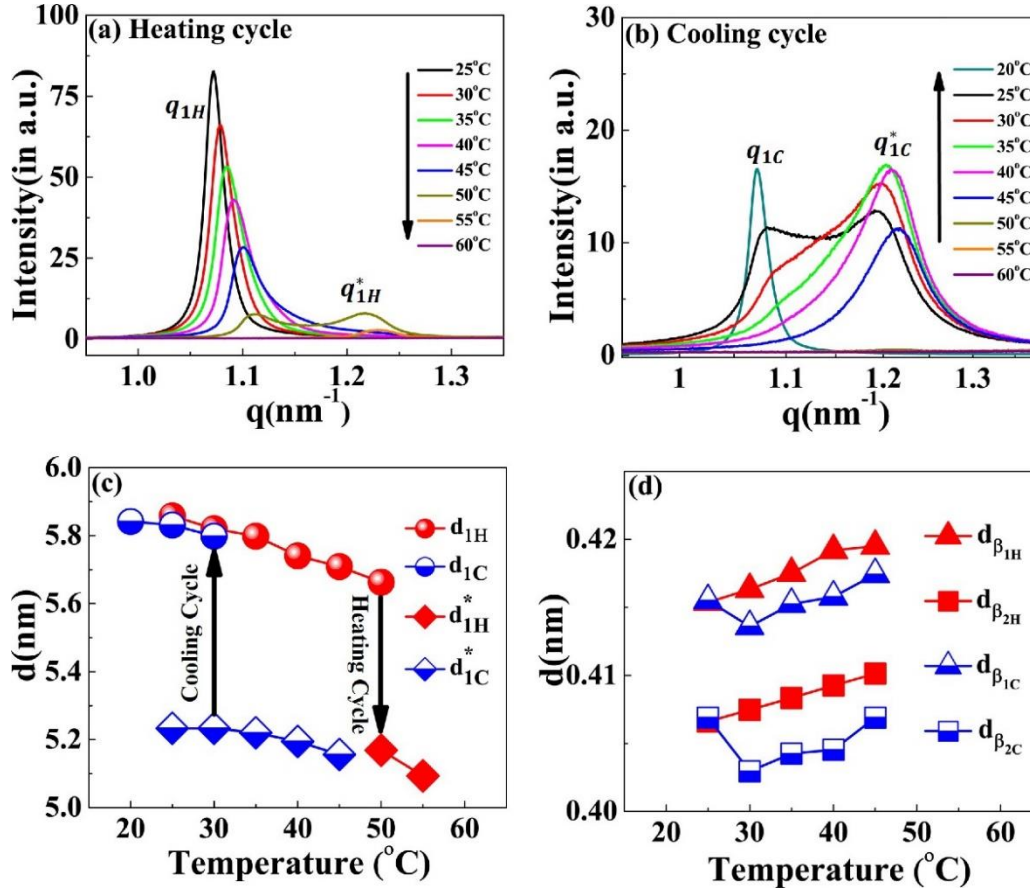


Figure 6. SAXS profiles of the $[V_7]_{40-48}$ h RLP at different temperatures during temperature cycle (a) heating and (b) cooling cycle. With an increase in temperature, the principal lamellar peak (q_{1H}) systematically moves toward higher q -values and splits at 50°C (q_{1H}^*) and both correlation peaks disappear at 60°C. During the cooling cycle, a correlation peak reappears at 50°C as q_{1C}^* , which denotes a thermal hysteresis of 15°C in the self-assembly. The peak q_{1C}^* splits to a daughter peak starting as a small hump at 35°C and becoming prominent at 30°C & 25°C. Variation in the interplanar distance (d in nm) during the heating-cooling cycle corresponding to correlation peaks (c) q_{1H} , q_{1H}^* , q_{1C} , and q_{1C}^* (d) q_{β_1} and q_{β_2} (β -sheet peaks) obtained by the relation $d = 2\pi/q$. Arrows in (c) indicate the temperatures at which the system transit to the two-nanoscale phase during the heating and cooling cycle.

Also, at 45°C, all the correlation peaks corresponding to a lamellar nanostructure (q_{1C}^* , q_{2C} , q_{4C} , where C in the superscript signifies the cool cycle) reappear, as well as the β -sheets (q_{β_1H} and q_{β_2H} , Supplementary Fig. S6). During further cooling, the lamellar peaks systematically shift to lower q -values

(Fig. 6b & Supplementary Fig. S6). In addition, starting at 35°C, and seen very clearly at 25°C, the peak splits into two reflections q_{1c}^* (1.07 nm⁻¹) and q_{1c} (1.19 nm⁻¹), similar to those observed in the heat cycle at 50°C.

Furthermore, lowering the temperature to 20° C diminishes the peak at q_{1c}^* while q_{1c} peak persists (Fig. 6b). The lamellar interplanar distance ($d = 2\pi/q$) hysteresis loop during the heating and cooling cycle is presented in Fig. 6c. We could detect only a weak anti-correlation between the temperature and the interplanar distance but could observe the coexistence of two nanoscopic phases at 50° C and 30° C for the heating and cooling cycles, respectively. Noticeably, the β -sheet spacing positively correlates with temperature between 25 to 45° C and disappears above this temperature (Fig. 6d).

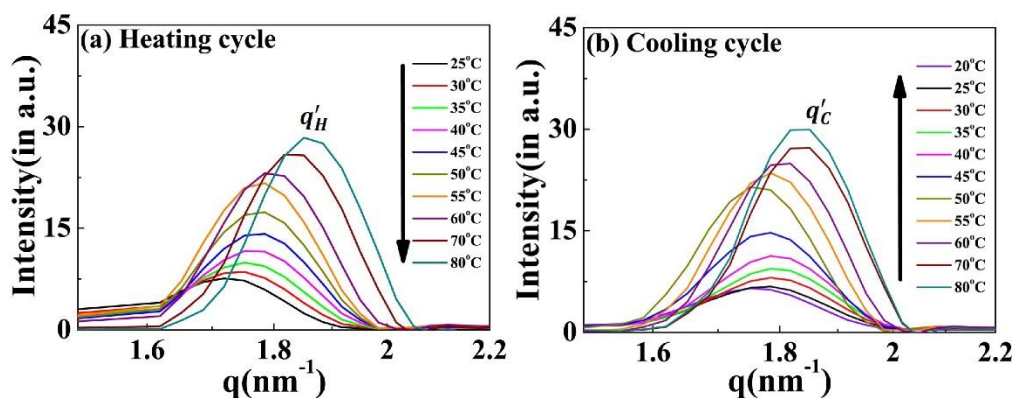


Figure 7. Scattering profiles of the $[V_7]_{40-48}$ h RLP exhibiting a variation in correlation peak q' as a function of temperature. Profiles during the (a) heating cycle (q'_H) and (b) cooling cycle (q'_C). The q' peak persists through all the temperature range examined, and the peak position is essentially independent of the heating and cooling cycle. The intensity of q' increases with an increase in temperature for both cycles.

The correlation peak designated as q' remains present throughout the complete heating-cooling cycle (Fig. 7a, b). Interestingly, the intensity of the q' peak is positively correlated with the temperature during both cycles, with the peak position (and hence the inter-planer distance) independent of the cycle direction (Supplementary Fig. S7). Both these findings differentiate this from the other nanoscopic structures and suggest that a discrete equilibrated state is present in the system.

We also performed temperature-dependent CD studies for $[V_7]_{40-48}$ h system with same experimental conditions as for SAXS measurements. Upon ramping the temperature from 20 to 80° C at a ramp rate of 5° C, we observed that the valleys at ~ 203 and 225 nm corresponding to β -sheets persist upto 60° C during heat cycle. These valleys almost vanish at 70 and 80° C (Supplementary Fig. S8a: for clarity we have shown results at interval of 10° C). During cool cycle the valleys reappeared at 60° C and persist upto 20° C (Supplementary Fig. S8b).

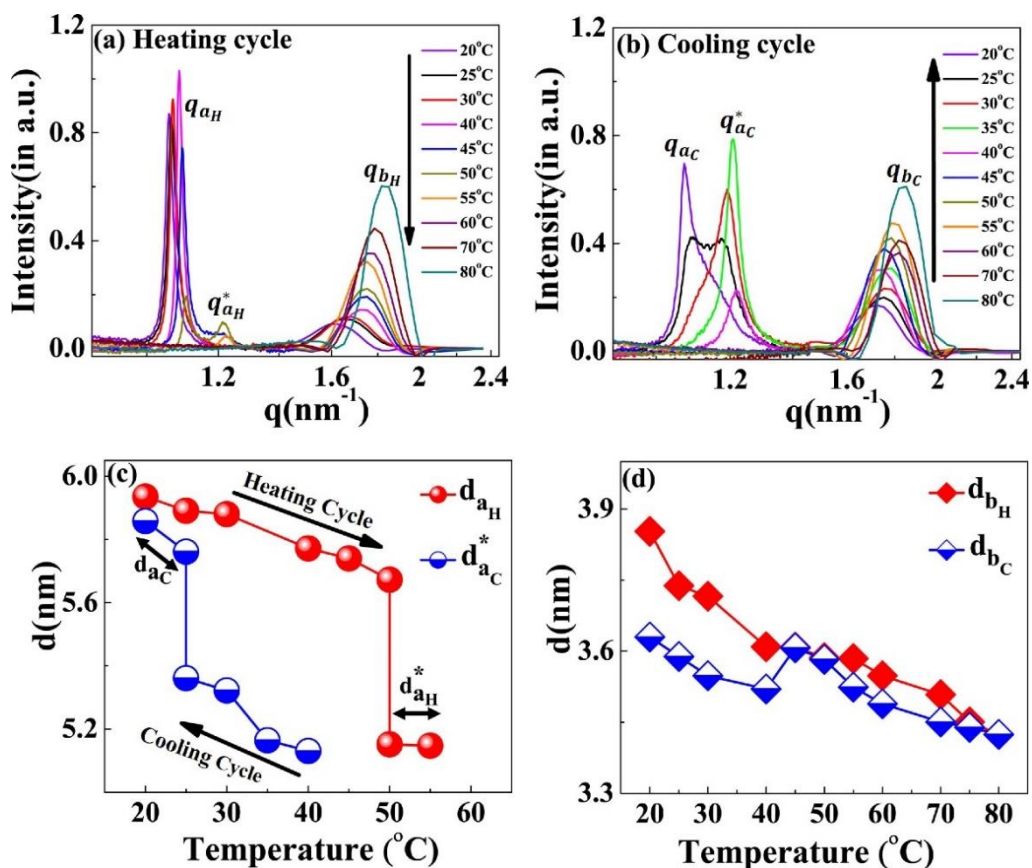


Figure 8. Scattering profiles of the [WT]₈₀-24 h sample at different temperatures. During the (a) heating and (b) cooling cycle. The correlation peaks q_a and q_b indicates short-range nanoscopic organization. Upon ramping the temperature from 20°C- 45°C, the peak q_{aH} shifts towards higher q -values, splits into a daughter peak (q_{aH}^*) at 50°C and both peaks disappear at 60°C. Upon cooling, the correlation peak reappears first at 40°C as q_{aC}^* . This exhibits a thermal hysteresis of 20°C in the self-assembly. Below 30°C, the q_{aC}^* diminishes and a new sharp correlation peak, q_{aC} appears at 20°C. Variations in the interplanar distance (d in nm) (c) d_a (d) d_b during the heating and cooling cycle. The system exhibits the presence of two-nanosopic phases characterized by two-interplanar distances, d_{aH} and d_{aH}^* at 50°C and 55°C during the heating cycle and by d_{aC} and d_{aC}^* at 25°C during the cooling cycle. The correlation peak q_b remains prominent throughout the heating-cooling cycle, with minimal changes in interplanar distance.

The scattering profiles of the [WT]_n RLPs with a variable number of octapeptide repeats after 24 h incubation at 80°C differ from that of [V₇]₄₀ RLP. We could not detect any correlation peaks in the scattering profiles where $n = 20, 40,$ and $60,$ (Supplementary Fig. S9), which indicates the absence of short-or-long range-order in these RLPs. However, the SAXS/WAXS profiles of the [WT]₈₀-24 h sample do contain two correlation peaks (Fig. 4b & Supplementary Fig. S10 (a) & (b)). These correlation peaks do not show corresponding higher-order reflections during both the heating and cooling cycle (Supplementary Fig. S10 (a) & (b)), thus preventing a description of the long-range symmetry. Noticeably the correlation peaks are rather sharp which suggests a homogeneous short-range correlation.

During the heating cycle of the [WT]_{80-24 h} sample, q_{aH} shifts systematically toward higher q -values and split into a daughter peak q_{aH}^* at 50°C (Fig. 8a) before both disappear at 55°C and 60°C respectively. In contrast, during the cooling cycle, the correlation peak (q_{aC}^*) reappears at 40°C (Fig. 8b). Upon further cooling below 30°C, the correlation peak q_{aC}^* diminishes and a new sharp correlation peak, $q_{aC} = 1.07 \text{ nm}^{-1}$ appears and becomes more prominent as the system cools down to 20°C (Fig. 8b). Thus, we can conclude that the disappearance of q_{aH}^* at 60°C during the heating cycle and the appearance of q_{aC} at 40°C in the cooling cycle are interrelated.

Similar to the results seen with [V₇]₄₀, the [WT]_{80-24 h} system exhibits thermal hysteresis of the nanoscopic structure (Fig. 8c). However, the exact short-range nanoscopic organization differs. While a previous report suggested that UCST SynIDPs like [WT]₈₀ show phase separation thermal hysteresis²⁰, our results demonstrate that nanoscale organization also exhibits such hysteretic behavior. In addition, the correlation peak q_b remains prominent with little alteration and minimal hysteresis throughout the entire heating and cooling cycle, as shown by minimal changes in the interplanar distance (Fig. 8d).

Discussion

The results presented here demonstrate modulation of the micro and nano self-assembly of resilin-like SynIDPs by periods of high-temperature incubation at 80°C and subsequent cooling. For the [WT]₄₀ and [WT]₈₀ RLPs, varying the incubation time correlates with a structural transition from micro-ellipsoids to rods structures. In contrast, the [V₇]₄₀ RLP, that has a V instead of Y amino acid at the 7th position of the GRGDSPYS repeat unit of WT RLP, requires a longer incubation time and only transitions from an amorphous coacervate to an ellipsoidal structure after 48 h at 80°C. Interestingly, upon cooling back to 25°C, prolonged incubation of both the [WT]₈₀, and [V₇]₄₀ RLPs at 80°C leads to the formation of hierarchical self-assembled nanostructures, an observation that was confirmed by the sharp X-ray scattering correlation peaks.

Based on their absorbance measurements, Quiroz et al.³⁴ reported that RLPs undergo loss of LLPS during multiple heating and cooling cycles around the UCST. They attributed such behavior to the formation of irreversible aggregates. A similar effect has also been observed for synthetic polymers exhibiting UCST phase behavior.⁵⁰ The loss of LLPS and the formation of irreversible pathological aggregates have also been observed in the low complexity disordered domain of RNA-binding protein FUS.⁵¹ IDPs of A β , tau and α -synuclein proteins in aqueous solution also form such irreversible aggregates.⁵² In line with these findings, we expect long incubations at 80°C to lead to a progressive build-up of irreversible aggregates in the [WT]₄₀ and [WT]₈₀ RLPs. Indeed, on the microscopic scale, we did observe various ellipsoidal

aggregates in the HRSEM images after long incubation times at 80°C (Figs. 1c, d & 2c, d). Moreover, these ellipsoidal aggregates systematically self-assemble to form rods in the [WT]₄₀ and [WT]₈₀ RLPs.

The driving force for this self-assembly could be the abundance of H-bond's forming amino acids aspartic acid (D), serine (S) and tyrosine (Y) that can create metastable interchain interactions. Thus, we suggest that a long incubation time promotes additional mixing in the liquid state that can overcome meta-stable states and accelerate the formation of self-assembled micro-scale structures via the hydrogen-bond's forming amino acids. These interactions could also explain the formation of interconnected nanofibers observed in these systems (Supplementary Fig S1).

Upon prolonged incubation at 80°C, the micro-ellipsoids aggregate throughout the nanofibers' connection to form rods or fiber-like structures. In contrast and supporting our hypothesis that intermolecular H-bonding is an important driving force for the hierarchical self-assembly in RLPs at higher temperatures is the lack of formation of interconnected fibers in [V₇]₄₀ RLP incubated for 48 h at 80°C. The [V₇]₄₀ RLP, has a non-H-bonding residue (V) instead of a H-bonding amino acid (Y). Further support is the reduction in the number of rods after prolonged 80°C incubation.

The incubation time also promotes order on the nanoscopic length scale in a sequence-dependent manner. The sequence of [V₇]₄₀ consists of a zwitterionic hydrophilic domain (i.e., GRGD), with positively charged arginine (R) and negatively charged aspartic acid (D). Each hydrophilic repeat is conjugated to a neutral-charged domain (i.e., SPVS) with a hydrophobic valine (V) residue. Thus, we presume that our sequence exhibits properties similar to amphiphilic polypeptides that possess alternating repeats of single hydrophilic and hydrophobic amino acids instead of alternating domains, each four amino acids long.^{53,54} Alternating amphiphilic peptides are known to form highly stable β -sheet structures in aqueous solution due to the interaction between their hydrophobic faces,⁵³ while random polymers of the same composition lead to α -helical structures.^{55,56} Indeed, our X-ray scattering and CD data (Figs. 4d & 5d) provide evidence of β -sheets in the [V₇]₄₀ RLP.

The [WT]₄₀ RLP also contains an alternating amphiphilic sequence (GRGDSPYS) with Y as a hydrophobic residue. Nonetheless, the CD spectra of the [WT]₄₀ system after 48 h incubation at high temperature still exhibits an α -helical structure. According to Chou-Fasman's potential scale, the valine has the highest propensity to form β -sheets⁵⁷, which can explain the presence of β -sheets in [V₇]₄₀ RLP. In agreement with our findings, molecular dynamic simulations of β -sheet formation in self-assembled peptide amphiphile fibers exhibits that fibers with a higher valine/alanine ratio have a higher percentage of β -sheet.⁵⁸ The molecular reason for the presence of α -helical structures in the WT system is however, unclear at this time.

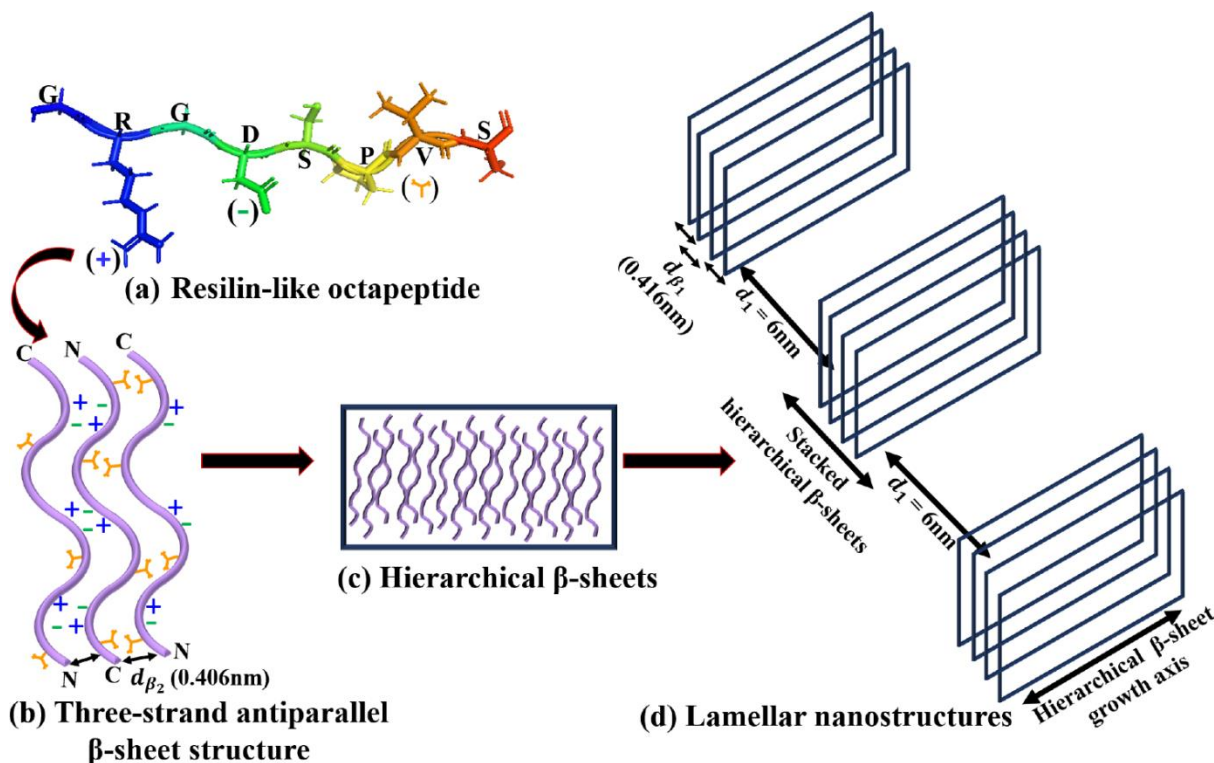


Figure 9. Schematic representation of self-assembly of hierarchical lamellar nanostructures in the $[V_7]_{40-48h}$ RLP (a) PyMOL structure of a single RLP unit GRGDSPVS having hydrophobic and hydrophilic domain due to the presence of arginine (R) and aspartic acid (D), and valine (V) amino acids respectively. The (+) and (-) represent the charges on R and D and used to denote these amino acids in (b). At the same time, the orange Y-shape symbol describes the hydrophobic valine (b) a three-strand antiparallel β -sheet structure formed due to the alternating arrangement of the ionic (R and D) and hydrophobic (V) amino side chains on each β -strand of the octapeptide repeat. The distance $d_{\beta_2} = 0.406$ nm represents the backbone H-bonding distance between antiparallel β -strands. (c) Hierarchical β -sheets formed by lateral stacking of three-strand antiparallel β -sheet structure. (d) Lamellar nanostructures having interplanar distance (d_1) of 6 nm formed by lateral arrangement of stacked hierarchical β -sheets. Each hierarchical β -sheet in a stack is separated by a distance of $d_{\beta_1} = 0.416$ nm from the other. d_1 , d_{β_1} and d_{β_2} are obtained from X-ray correlation peaks.

Notably, the alternating amphiphilic sequence with valine is insufficient to induce β -sheet formation, which requires a prolonged incubation time (i.e., 48 h) at a high temperature (80°C). We attributed this finding to a rough but shallow energy landscape at high temperatures with alternative transient metastable minima of random coils and α -helix. A prolonged incubation allows the system to equilibrate to the lowest β -sheet energy state.⁵⁹ Thus, the major driving force for β -sheets is the self-interaction between the hydrophobic valine side chains on neighboring peptides, which minimizes unfavorable contact with water molecules. The self-complementary ion pair interactions between the alternate positively charged arginine (R) and negatively charged aspartic acid (D) motifs may also assist in stabilizing β -sheet formation.

Apparently, incubation up to 48 h is insufficient to induce β -sheets in the [WT]₄₀ RLP, which shares identical ionic pairing.

In Fig. 9a we show schematic representation of resilin-like octapeptide unit GRGDSPVS having hydrophobic and hydrophilic domains due to the presence of arginine (R) and aspartic acid (D), and valine (V) amino acids, respectively. In [V₇]₄₀ RLP, the adjacent polypeptide chains (β -strands) in the β -sheets are knitted in an antiparallel fashion through a backbone stabilized via hydrogen bonds separated by a distance of $d_{\beta_2} = 0.406$ nm. Due to the amphiphilic nature of our system, the valine side chains of two neighboring β -strands can interact with each other to form a hydrophobic face on the side of the sheets away from the water molecules. On the other side of the sheet, electrostatic interactions between complementary ionic amino acid pairs stabilize a three-strand β -sheet structure (Fig. 9b). Such an arrangement has previously been reported for the alternating amphiphilic oligopeptide (EAK)₁₆, which possesses a complementary ion-pair in the sequence.⁶⁰ As another example, the peptide (VK)₄VPPT(KV)₄ exhibits the formation of self-assembled fibrils due to the presence polar β -sheet with distinctive hydrophobic (V) and hydrophilic (K) domains. β -sheets of this peptide collapse into fibrils due to collapse of hydrophobic domains. Further, molecular dynamics simulation of the amphiphilic peptides I₄K₂ and KI₄K indicated that the non-bonded energies of the three-strand β -sheets are three times lower than that of individual monomers.⁶¹

At high peptide concentration, the three-stranded structure can laterally self-assemble via Van der Waals interactions to form correlated hierarchical β -sheets (Fig. 9c). Indeed, at low temperatures, the [V₇]₄₀ RLP shows a well-ordered lamellar morphology after 48 h of incubation, as evidenced by sharp correlation peaks in its X-ray scattering profiles, as well as anti-parallel β -sheet signatures. Spider silk fibers, whose sequence is also amphiphilic with highly conserved poly-(Ala-Gly) and poly-Ala repeats, similarly contain crosslinked nanoscale crystals of antiparallel β -sheets structures.⁶²⁻⁶⁴ These nanocrystals are further embedded in a semi-amorphous phase of less orderly structures, helices, and β -turns. Therefore, we conclude that the formation of lamellar structures in the [V₇]₄₀ RLP is due to the alternate arrangement of antiparallel β -sheets at a distance of ~ 6 nm. This arrangement is similar to silk's, but in our [V₇]₄₀ RLP, the β -sheets self-assemble to form a lamellar nanostructure instead of fibers (Fig. 9d).

Of note, we also observed that high temperature diminishes the self-assembled nanoscopic structures in the [V₇]₄₀ and [WT]₈₀ RLPs in a hysteretic manner. Previous reports suggest that IDPs exhibit temperature-dependent collapse, quantified as a decrease in their radius of gyration.⁶⁵⁻⁶⁷ This temperature-induced collapse in IDPs implies the presence of temperature-dependent interactions such as hydrophobic effects^{68,69} or changes in solvation-free energy.³⁰ Interestingly, Wuttke et al.⁷⁰ reported that the most

hydrophilic and charged IDP sequences exhibit a significant temperature-induced collapse. They also suggested that along with the classical hydrophobic effects, the temperature-dependent solvation-free energies of the hydrophilic amino acids play a vital role in determining the collapse. Zerge et al.⁷¹ simulated the solvent-accessible surface area (SASA) and showed that this was decreased by hydrophobic amino acids up to a critical temperature and then subsequently increased. For negatively charged amino acids (Asp;D and Glu; E), the SASA decreases with increasing temperature, which avoids water contact, while the cationic amino acid arginine(R) exhibits the opposite tendency.^{70,71} Therefore, the temperature-dependent self-assembly in our [V₇]₄₀ and [WT]₈₀ RLPs can be attributed to the collapse of the valine (V) or tyrosine (Y) domains due to the enhanced hydrophobic effect caused by an increase in temperature. Since the RLPs have R and D residues, which exhibit opposing SASA temperature dependencies, we might expect the combined temperature dependency to be more complex and require further investigation.

Summary

We have demonstrated that it is possible to modulate the hierarchical self-assembly in RLPs by simply adjusting the time of incubation at high temperatures. We also witnessed a temperature-dependent hysteresis in the self-assembled nanostructure of these SynIDPs that is determined by their sequence, and suggest that the lamellar nanostructures formed in this system are associated with the presence of β -sheets. A variation in incubation time also induced structural transitions from amorphous to rod/ellipsoids during the LLPS of these SynIDPs. In conclusion, our results introduce a new approach to access new forms of self-assembled structures by the interplay between the incubation time and hysteresis of these SynIDPs. The micro-phase separated nanoscale lamellar or short-range ordered structure observed in our RLPs can find application in heterogeneous catalysis, drug delivery and scaffolds to guide tissue regeneration, similar to block copolypeptides.

Materials and Methods

Protein Purification

The RLPs were recombinantly expressed from plasmid-borne genes in *E. coli*, and were purified as reported previously.²⁰ Briefly, *E. coli* (BL21) cells were grown overnight in Terrific Broth (TB) culture medium, followed by induction with 500 μ M IPTG. The bacteria were pelleted at 3500 RCF, resuspended in PBS, then lysed by sonication and centrifuged at 4°C to separate the supernatant and pellet containing the RLP of interest. The pellets were suspended in an equal volume of 8M urea in 150 mM PBS buffer and heated for 10 min in a water bath maintained at 37°C, followed by centrifugation at 20,000 RCF for 20 min. The collected supernatants were dialyzed against milli-Q water at 4°C for 48 h with two changes of dialysis water. The suspension obtained after dialysis was centrifuged at 3500 RCF for 10 min at 4°C to pellet the RLP. The protein pellets were then lyophilized for three days to obtain dry RLP and stored at -80°C as powder. The molecular weight and purity of each protein was confirmed by matrix-assisted laser desorption/ionization time of flight mass spectrometry (MALDI-TOF-MS). The experimental m/z obtained for [WT]₄₀, [V₇]₄₀ and [WT]₈₀ samples are 33379, 30839 and 66193 respectively (Supplementary Fig. S11(a)-(c)).

Sample preparation

For small and wide-angle X-ray studies (SAXS and WAXS), buffers for background subtraction were prepared for each RLP by using slide-A-lyzer MINI dialysis devices (3.5K MWCO). A 100 μ M solution of each RLP, prepared in 2mL phosphate buffer (150 mM, at pH 7), was incubated at 60°C for 15 min. The hot solution was transferred to the MINI dialysis tubes and dialyzed against 50 mL of phosphate buffer for 4-5 h at 60°C on a shaker. Maintaining a temperature above the T_i (i.e., 40°C) was necessary to prevent phase separation. We secured the mouth of the dialysis tube with a cellophane sheet to prevent evaporation of the buffer, and the tube was further closed with the cap. The dialyzed buffers were stored at 4°C and used for SAXS measurements as required.

For the RLP measurements, we used 100 μ M dialyzed RLP solutions of [WT]₄₀, [WT]₈₀, and [V₇]₄₀ in triplicate. We heated the RLP solutions at 80°C on a heating bath for an incubation time of 1, 24, or 48 h. We defined the samples based on RLP name and incubation time. For example, samples of [WT]₄₀ RLP

heated at 80°C for 1, 24, and 48 h are referred to as [WT]_{40-1 h}, [WT]_{40-24 h}, and [WT]_{40-48 h}, respectively. Detailed material and methods are given in supporting information.

Data Availability

All data generated or analyzed during this study are included in this published article.

References

1. Gomes, E. & Shorter, J. The molecular language of membraneless organelles. *J. Biol. Chem.* **294**, 7115–7127 (2019).
2. Uversky, V. N. Intrinsically disordered proteins in overcrowded milieu: Membrane-less organelles, phase separation, and intrinsic disorder. *Curr. Opin. Struct. Biol.* **44**, 18–30 (2017).
3. Marnik, E. A. & Updike, D. L. Membraneless organelles: P granules in *Caenorhabditis elegans*. *Traffic* **20**, 373–379 (2019).
4. Habchi, J., Tompa, P., Longhi, S. & Uversky, V. N. Introducing protein intrinsic disorder. *Chem. Rev.* **114**, 6561–6588 (2014).
5. Ehm, T. *et al.* Intrinsically disordered proteins at the nano-scale. *Nano Futur.* **5**, 022501 (2021).
6. Uversky, V. N. & Kulkarni, P. Intrinsically disordered proteins: Chronology of a discovery. *Biophys. Chem.* **279**, 106694 (2021).
7. Chakrabarti, P. & Chakravarty, D. Intrinsically disordered proteins/regions and insight into their biomolecular interactions. *Biophys. Chem.* **283**, 106769 (2022).
8. Galea, C. A., Wang, Y., Sivakolundu, S. G. & Kriwacki, R. W. Regulation of cell division by intrinsically unstructured proteins: Intrinsic flexibility, modularity, and signaling conduits. *Biochemistry* **47**, 7598–7609 (2008).
9. Van Roey, K., Gibson, T. J. & Davey, N. E. Motif switches: decision-making in cell regulation. *Curr. Opin. Struct. Biol.* **22**, 378–385 (2012).
10. Gsponer, J., Futschik, M. E., Teichmann, S. A. & Babu, M. M. Tight regulation of unstructured proteins: From transcript synthesis to protein degradation. *Science (80-.)*. **322**, 1365–1368 (2008).

11. Dunker, A. K., Cortese, M. S., Romero, P., Iakoucheva, L. M. & Uversky, V. N. Flexible nets. The roles of intrinsic disorder in protein interaction networks. *FEBS J.* **272**, 5129–5148 (2005).
12. Kim, P. M., Sboner, A., Xia, Y. & Gerstein, M. The role of disorder in interaction networks: A structural analysis. *Mol. Syst. Biol.* **4**, 179 (2008).
13. Iakoucheva, L. M., Brown, C. J., Lawson, J. D., Obradović, Z. & Dunker, A. K. Intrinsic Disorder in Cell-signaling and Cancer-associated Proteins. *J. Mol. Biol.* **323**, 573–584 (2002).
14. Chong, P. A. & Forman-Kay, J. D. Liquid–liquid phase separation in cellular signaling systems. *Curr. Opin. Struct. Biol.* **41**, 180–186 (2016).
15. Cuevas-Velazquez, C. L. & Dinneny, J. R. Organization out of disorder: liquid–liquid phase separation in plants. *Curr. Opin. Plant Biol.* **45**, 68–74 (2018).
16. Abyzov, A., Blackledge, M. & Zweckstetter, M. Conformational Dynamics of Intrinsically Disordered Proteins Regulate Biomolecular Condensate Chemistry. *Chem. Rev.* **122**, 6719–6748 (2022).
17. Babinchak, W. M. & Surewicz, W. K. Liquid–Liquid Phase Separation and Its Mechanistic Role in Pathological Protein Aggregation. *J. Mol. Biol.* **432**, 1910–1925 (2020).
18. Alberti, S. & Dormann, D. Liquid-Liquid Phase Separation in Disease. *Annu. Rev. Genet.* **53**, 171–194 (2019).
19. Ray, S. *et al.* α -Synuclein aggregation nucleates through liquid–liquid phase separation. *Nat. Chem.* **2020 128** **12**, 705–716 (2020).
20. Dzuricky, M., Rogers, B. A., Shahid, A., Cremer, P. S. & Chilkoti, A. De novo engineering of intracellular condensates using artificial disordered proteins. *Nat. Chem.* **12**, 814–825 (2020).
21. Indulkar, A. S., Box, K. J., Taylor, R., Ruiz, R. & Taylor, L. S. pH-dependent liquid–liquid phase separation of highly supersaturated solutions of weakly basic drugs. *ACS Publ.* **12**, 2365–2377 (2015).
22. Indulkar, A. S., Gao, Y., Raina, S. A., Zhang, G. G. Z. & Taylor, L. S. Exploiting the Phenomenon of Liquid-Liquid Phase Separation for Enhanced and Sustained Membrane Transport of a Poorly Water-Soluble Drug. *Mol. Pharm.* **13**, 2059–2069 (2016).

23. Sun, M., Shichao, D., Tang, W., Jia, L. & Gong, J. Design of Spherical Crystallization for Drugs Based on Thermal-Induced Liquid-Liquid Phase Separation: Case Studies of Water-Insoluble Drugs. *Ind. Eng. Chem. Res.* (2019).
24. Liu, J., Zhorabek, F., Dai, X., Huang, J. & Chau, Y. Minimalist Design of an Intrinsically Disordered Protein-Mimicking Scaffold for an Artificial Membraneless Organelle. *ACS Cent. Sci.* **8**, 493–500 (2022).
25. Mu, W. *et al.* Membrane-confined liquid-liquid phase separation toward artificial organelles. *Sci. Adv.* **7**, 9000–9028 (2021).
26. Simmel, F. C. Synthetic organelles. *Emerg. Top. Life Sci.* **3**, 587–595 (2019).
27. Costa, S. A. *et al.* Photo-Crosslinkable Unnatural Amino Acids Enable Facile Synthesis of Thermoresponsive Nano- to Microgels of Intrinsically Disordered Polypeptides. *Adv. Mater.* **30**, 1704878 (2018).
28. Ibáñez-Fonseca, A., Flora, T., Acosta, S. & Rodríguez-Cabello, J. C. Trends in the design and use of elastin-like recombinamers as biomaterials. *Matrix Biol.* **84**, 111–126 (2019).
29. Tikhonova, T. N. *et al.* Tunable Self-Assembled Peptide Hydrogel Sensor for Pharma Cold Supply Chain. *ACS Appl. Mater. Interfaces* **14**, 55392–55401 (2022).
30. Dignon, G. L., Best, R. B. & Mittal, J. Biomolecular phase separation: From molecular driving forces to macroscopic properties. *Annu. Rev. Phys. Chem.* **71**, 53–75 (2020).
31. Seuring, J. & Agarwal, S. Polymers with upper critical solution temperature in aqueous solution: Unexpected properties from known building blocks. *ACS Macro Lett.* **2**, 597–600 (2013).
32. Holehouse, A. S. & Pappu, R. V. Collapse Transitions of Proteins and the Interplay among Backbone, Sidechain, and Solvent Interactions. *Annu. Rev. Biophys.* **47**, 19–39 (2018).
33. Moses, D. *et al.* Revealing the Hidden Sensitivity of Intrinsically Disordered Proteins to their Chemical Environment. *J. Phys. Chem. Lett.* **11**, 10131–10136 (2020).
34. Quiroz, F. G. *et al.* Intrinsically disordered proteins access a range of hysteretic phase separation behaviors. *Sci. Adv.* **5**, 5177–5195 (2019).

35. Qin, G., Hu, X., Cebe, P. & Kaplan, D. L. Mechanism of resilin elasticity. *Nat. Commun.* 2012 31 **3**, 1–9 (2012).
36. Wise, S. G. *et al.* Tropoelastin - a versatile, bioactive assembly module. *Acta Biomater.* **10**, 1532 (2014).
37. Balu, R., Dutta, N. K., Dutta, A. K. & Choudhury, N. R. Resilin-mimetics as a smart biomaterial platform for biomedical applications. *Nat. Commun.* 2021 121 **12**, 1–15 (2021).
38. Kornreich, M., Avinery, R. & Beck, R. Modern X-ray scattering studies of complex biological systems. *Curr. Opin. Biotechnol.* **24**, 716–723 (2013).
39. Li, T., Senesi, A. J. & Lee, B. Small Angle X-ray Scattering for Nanoparticle Research. *Chem. Rev.* **116**, 11128–11180 (2016).
40. Masunaga, H., Sakurai, K., Akiba, I., Ito, K. & Takata, M. Accurate measurements of intrinsic scattering from window materials by use of a vacuum camera. *J. Appl. Cryst.* **46**, 577–579 (2013).
41. Atkins, E. D. T., Keller, A. & Sadler, D. M. Structure analysis of chain-folded lamellar polyamide crystals from X-ray diffraction. *J. Polym. Sci. Part A-2 Polym. Phys.* **10**, 863–875 (1972).
42. Magill, J. H., Girolamo, M. & Keller, A. Crystallization and morphology of nylon-6,6 crystals: 1. Solution crystallization and solution annealing behaviour. *Polymer (Guildf)*. **22**, 43–55 (1981).
43. Lotz, B. Rippled Sheets: The Early Polyglycine Days and Recent Developments in Nylons. *ChemBioChem* **23**, e202100658 (2022).
44. Riekkel, C. & Vollrath, F. Spider silk fibre extrusion: combined wide- and small-angle X-ray microdiffraction experiments. *Int. J. Biol. Macromol.* **29**, 203–210 (2001).
45. Nagy, G., Igaev, M., Jones, N. C., Hoffmann, S. V. & Grubmüller, H. SESCA: Predicting Circular Dichroism Spectra from Protein Molecular Structures. *J. Chem. Theory Comput.* **15**, 5087–5102 (2019).
46. Micsonai, A., Bulyáki, É. & Kardos, J. BeStSel: From Secondary Structure Analysis to Protein Fold Prediction by Circular Dichroism Spectroscopy. *Methods Mol. Biol.* **2199**, 175–189 (2021).
47. Drummy, L. F., Phillips, D. M., Stone, M. O., Farmer, B. L. & Naik, R. J. Thermally induced α -

- helix to β -sheet transition in regenerated silk fibers and films. *Biomacromolecules* **6**, 3328–3333 (2005).
48. Kong, J. & Yu, S. Fourier Transform Infrared Spectroscopic Analysis of Protein Secondary Structures. *Acta Biochim. Biophys. Sin. (Shanghai)*. **39**, 549–559 (2007).
 49. Jumper, J. *et al.* Highly accurate protein structure prediction with AlphaFold. *Nat.* 2021 5967873 **596**, 583–589 (2021).
 50. Seuring, J. & Agarwal, S. First example of a universal and cost-effective approach: Polymers with tunable upper critical solution temperature in water and electrolyte solution. *Macromolecules* **45**, 3910–3918 (2012).
 51. Shin, Y. *et al.* Spatiotemporal Control of Intracellular Phase Transitions Using Light-Activated optoDroplets. *Cell* **168**, 159–171 (2017).
 52. Nguyen, P. H. & Derreumaux, P. Structures of the intrinsically disordered A β , tau and α -synuclein proteins in aqueous solution from computer simulations. *Biophys. Chem.* **264**, 106421- (2020).
 53. Fukushima, Y. Synthesis and Highly Stable β -Sheet Formation of Sequential Alternating Amphiphilic Polypeptides. *Polym. J.* **28**, 113–120 (1996).
 54. Seipke, G., Arfmann, H. -A & Wagner, K. G. Synthesis and properties of alternating poly(Lys-Phe) and comparison with the random copolymer poly(Lys51, Phe49). *Biopolymers* **13**, 1621–1633 (1974).
 55. Brack, A. & Spach, G. Multiconformational Synthetic Polypeptides. *J. Am. Chem. Soc.* **103**, 6319–6323 (1981).
 56. Brack, A. & Caille, A. SYNTHESIS AND β -CONFORMATION OF COPOLYPEPTIDES WITH ALTERNATING HYDROPHILIC AND HYDROPHOBIC RESIDUES. *Int. J. Pept. Protein Res.* **11**, 128–139 (1978).
 57. Prevelige, P. & Fasman, G. D. Chou-Fasman Prediction of the Secondary Structure of Proteins. *Predict. Protein Struct. Princ. Protein Conform.* 391–416 (1989).
 58. Lee, O. S., Liu, Y. & Schatz, G. C. Molecular dynamics simulation of β -sheet formation in self-assembled peptide amphiphile fibers. *J. Nanoparticle Res.* **14**, (2012).

59. Bryngelson, J. D., Onuchic, J. N., Socci, N. D. & Wolynes, P. G. Funnels, pathways, and the energy landscape of protein folding: A synthesis. *Proteins Struct. Funct. Bioinforma.* **21**, 167–195 (1995).
60. Zhang, S., Lockshin, C., Cook, R. & Rich, A. Unusually stable β -sheet formation in an ionic self-complementary oligopeptide. *Biopolymers* **34**, 663–672 (1994).
61. Zhao, Y. *et al.* Tuning the self-assembly of short peptides via sequence variations. *ACS Publ.* **29**, 13457–13464 (2013).
62. Van Beek, J. D., Hesst, S., Vollrath, F. & Meier, B. H. The molecular structure of spider dragline silk: Folding and orientation of the protein backbone. *Proc. Natl. Acad. Sci. U. S. A.* **99**, 10266–10271 (2002).
63. Lefèvre, T., Rousseau, M. E. & Pézolet, M. Protein Secondary Structure and Orientation in Silk as Revealed by Raman Spectromicroscopy. *Biophys. J.* **92**, 2885–2895 (2007).
64. Nova, A., Keten, S., Pugno, N. M., Redaelli, A. & Buehler, M. J. Molecular and nanostructural mechanisms of deformation, strength and toughness of spider silk fibrils. *Nano Lett.* **10**, 2626–2634 (2010).
65. Makhatadze, G. I. & Privalov, P. L. Protein interactions with urea and guanidinium chloride: A calorimetric study. *J. Mol. Biol.* **226**, 491–505 (1992).
66. Nettels, D. *et al.* Single-molecule spectroscopy of the temperature-induced collapse of unfolded proteins. *Proc. Natl. Acad. Sci. U. S. A.* **106**, 20740–20745 (2009).
67. Langridge, T. D., Tarver, M. J. & Whitten, S. T. Temperature effects on the hydrodynamic radius of the intrinsically disordered N-terminal region of the p53 protein. *Proteins Struct. Funct. Bioinforma.* **82**, 668–678 (2014).
68. Hummer, G., Garde, S., García, A. E., Pohorille, A. & Pratt, L. R. An information theory model of hydrophobic interactions. *Proc. Natl. Acad. Sci.* **93**, 8951–8955 (1996).
69. Chandler, D. Interfaces and the driving force of hydrophobic assembly. *Nat.* 2005 4377059 **437**, 640–647 (2005).
70. Wuttke, R. *et al.* Temperature-dependent solvation modulates the dimensions of disordered

proteins. *Proc. Natl. Acad. Sci. U. S. A.* **111**, 5213–5218 (2014).

71. Zerze, G. H., Best, R. B. & Mittal, J. Sequence- and Temperature-Dependent Properties of Unfolded and Disordered Proteins from Atomistic Simulations. *J. Phys. Chem. B* **119**, 14622–14630 (2015).

Author Information

V.S. and R.B. designed the experiments and wrote the manuscript. V.S. prepared all the figures for the manuscript and conducted SAXS and CD measurements and analysis. S.M. assisted in the synchrotron SAXS's measurements. V.S., D.C.G., G.K. and L.A.A. conducted the HRSEM and FTIR measurements. M.N., Y.S. and A.C. purified the proteins and conducted Mass spectroscopic measurements. All the authors reviewed and refined the manuscript.

Corresponding Author

*roy@tauex.tau.ac.il.

Acknowledgments

The synchrotron SAXS/WAXS data were collected on a beamline I22 at Diamond Light Source, Oxford, United Kingdom. We would like to thank beamline scientists Dr. Nick Terrill and Dr. Andy Smith for their assistance in using the beamlines. This work was supported by the National Science Foundation under Grant No. 1715627, the United States-Israel Bi-national Science Foundation under Grant No. 2020787, and the Israel Science Foundation under Grants No. 1454/20 to R.B, and by the NIH through Grant No. R35GM127042 and the AFOSR through Grant No. FA9550-20-1-0241 (SUB0000436) to A.C. D.C.-G. acknowledges the Marian Gertner Institute for Medical Nano systems at Tel Aviv University. D.C.-G. gratefully acknowledges the support of the Colton Foundation. The authors acknowledge the Chaoul Center for Nanoscale Systems at Tel Aviv University and the ADAMA Center for Novel Delivery Systems in Crop Protections for the use of instruments and staff assistance.

Competing Interest

The authors declare no competing interests.

